

Ultra-Broadband and High-Dynamic-Range THz Time-Domain Spectroscopy System Based on Organic Crystal Emitter and Detector in Transmission and Reflection Geometry

Uros Puc, Tobias Bach, Peter Günter, Marko Zgonik, and Mojca Jazbinsek*

The terahertz range of the electromagnetic spectrum reveals important insights when studying material properties. An ultra-broadband terahertz time-domain spectroscopy system based on state-of-the-art, high-stability organic nonlinear optical crystals used as both THz wave generator and detector is presented. In transmission geometry, a broad spectrum exceeding 20 THz and a high dynamic range of more than 80 dB is achieved using a compact 100 MHz femtosecond laser working at telecom wavelength 1560 nm. In the normal-incidence reflection geometry, a similar bandwidth with a dynamic range surpassing 60 dB is reported. The experimental results are supported by a complete theoretical model, which includes the pump pulse duration, THz phonon/vibrational modes of the organic crystals and optical/THz beam path optimizations. The effectiveness of the newly developed system is demonstrated by measuring pharmaceutical samples with distinct THz features in the ultra-broadband THz range and by measuring narrow water vapor lines at a spectral resolution of 2.7 GHz (0.090 cm^{-1}), resulting in an excellent accuracy with a frequency deviation of less than 0.05% from the reference values.

1. Introduction


Over the past few decades, the generation and detection of broadband terahertz waves in the frequency range 0.1–30 THz have seen tremendous progress, both in the achievable bandwidths and in the generated THz intensities.^[1,2] Most of the progress has relied on rapid advances in ultrafast laser sources, techniques, and novel materials. Pulsed broadband THz sources are widely used in today's THz time-domain spectroscopy (THz TDS) systems. For such systems, two main principles of THz wave generation are commonly used: photoconductive antennas^[3] that generate THz pulses by transient photocarriers induced by femtosecond pulses, whereas the second principle used here exploits optical rectification^[4] as a second-order nonlinear optical (NLO) effect in NLO materials. The Fourier transform-

limited femtosecond pulse duration defines the maximum bandwidth of the THz system. Besides this limit, other factors must be considered. In case of the photoconductive antennas, the main limiting factor is the recombination time of the photoinduced carriers in the photoconductor, typically being in the subpicosecond range. Due to these limitations, bandwidths beyond 6 THz are rarely achieved with the most typically used low-temperature-grown gallium arsenide (LT-GaAs) photoconductive antenna generators and detectors. On the other hand, NLO materials phase matching between the near-infrared pump beam and the generated THz field is essential in order for the generation process to be efficient.^[5] For organic NLO materials, due to the intrinsically lower dielectric dispersion from the lower THz frequency to the optical range, phase matching in a much broader THz range (tens of THz) is in principle possible in contrast to inorganic alternatives such as ZnTe, GaP, or LiNbO₃.^[6] Organic NLO crystals compared with polymers show excellent long-term stability and a high damage threshold ($>20 \text{ mJ cm}^{-2}$ at 1500 nm), allowing to use powerful pump lasers resulting in very intense THz fields beyond 8 GV m^{-1} generated with these materials.^[7–9] Often a higher bandwidth can be already achieved in a combined approach using organic or inorganic NLO material as a THz generator and a photoconductive

Dr. U. Puc, Dr. T. Bach, Dr. M. Jazbinsek
Institute of Computational Physics
Zurich University of Applied Sciences (ZHAW)
Winterthur, Switzerland
E-mail: mojca.jazbinsek@zhaw.ch

Prof. P. Günter
Swiss Federal Institute of Technology
ETH Zurich
Zurich, Switzerland

Prof. M. Zgonik
Faculty of Mathematics and Physics
University of Ljubljana
Ljubljana, Slovenia

 The ORCID identification number(s) for the author(s) of this article can be found under <https://doi.org/10.1002/adpr.202000098>.

© 2021 The Authors. Advanced Photonics Research published by Wiley-VCH GmbH. This is an open access article under the terms of the Creative Commons Attribution License, which permits use, distribution and reproduction in any medium, provided the original work is properly cited.

DOI: 10.1002/adpr.202000098

antenna as a THz detector, therefore reaching frequencies up to 8^[10] and 20 THz^[11] or even 60 THz.^[12] However, the broadband performance in these systems results in a low signal-to-noise ratio (SNR), especially at higher frequencies, therefore limiting their usability. In terms of SNR and sensitivity, both principles can achieve similar performance at lower THz frequencies. However, the electro-optic detection principle gives a better SNR at higher THz frequencies in comparison with photoconductive antennas which have bandwidth limitations due to substrate absorption losses at higher frequencies.^[3,13,14] Nowadays, commercial fiber-coupled THz TDS systems based on photoconductive antenna emitters and detectors are widely used in scientific and industrial applications, mainly due to their simplicity. Thus, such systems are able to achieve a broadband THz spectrum up to 6 THz and a high dynamic range up to 90 dB at sub-THz frequencies.^[15] Other THz principles capable of generating and detecting broadband THz radiation exist, among them air–plasma sources and air-based detection techniques,^[16] requiring powerful and bulky lasers and still exhibiting limited SNR at higher frequencies. Recently, progress was also made in spintronic THz emission achieving gapless spectrum in the 1–30 THz range^[17] and Ge-based emitters reaching frequencies up to 70 THz^[18] although at a lower SNR than in the established commercial systems.

Here we present an ultra-broadband, high dynamic range and compact THz TDS system based on 4-*N,N*-dimethylamino-4'-*N'*-methyl-stilbazolium tosylate (DAST) and 4-*N,N*-dimethylamino-4'-*N'*-methyl-stilbazolium 2,4,6-trimethylbenzenesulfonate (DSTMS) organic NLO crystals used for both generation and detection of THz pulses, using a relatively low-cost, low pulse energy and compact femtosecond lasers working at telecom wavelength 1560 nm and a high repetition rate of 40 or 100 MHz. Although most of the literature reports on organic NLO crystals pumped by high pulse energy (up to millijoule range), demanding bulky and expensive femtosecond laser systems, they may still only reach a limited few THz usable bandwidth limited mostly by conventional inorganic THz detection. We show here that superior performance in both bandwidth and dynamic range is achievable with organic NLO crystals when used as both generator and detector of THz waves in an optimized optical/THz system, even for pulse energies in the nanojoule range. In the transmission geometry, a peak dynamic range of more than 80 dB is demonstrated at 4 THz, still being above 70 dB at around 10 THz. Besides the ultra-broadband transmission geometry of the THz TDS system, we present the normal-incidence reflection geometry THz TDS system, where we demonstrate similar bandwidths and high dynamic range with the same detection principle. The theoretical model and optimization are in good agreement with the obtained experimental results. No degradation of the organic crystals used has been observed in our experimental setups at room temperature and humidity conditions. The validation of the newly developed system is done by measuring the water vapor lines with a high resolution of 2.7 GHz. We demonstrate an excellent frequency agreement with the reference HITRAN database, which is within less than 0.05% over the whole spectral range. In addition, we investigate pharmaceutical substances with spectral features in the frequency range of 1–20 THz to confirm the effectiveness of the ultra-broadband THz TDS system.

2. Organic Crystals and THz TDS Setup

2.1. Organic NLO Crystals

We used either the conventional DAST^[6] or the more recently developed DSTMS^[19] organic NLO crystals for the generation and detection of THz pulses. Organic crystals have excellent phase-matching characteristics and one order of magnitude higher electro-optic coefficient in comparison with more commonly used inorganic crystals such as ZnTe, GaAs, and GaP.^[16,20] DAST and DSTMS are analogous crystals with similar optical and NLO properties, e.g., an electro-optic coefficient of 47 and 49 pm V⁻¹ at 1500 nm, respectively.^[4,21] The crystal thicknesses in the range of 0.5–0.8 mm were used and the exact thicknesses are given next to each result in Section 4. As discussed in Section 3, these thicknesses are expected to be in the optimal range for THz generation and detection in our setup and no substantial differences were observed experimentally when changing the thickness in the above range (0.5–0.8 mm). DAST and DSTMS show best phase matching for THz wave generation in the 1300–1600 nm pump wavelength range, which is optimal for compact femtosecond lasers in the telecom wavelength range.^[7] The organic crystals used in this work were produced by the company Rainbow Photonics AG, Zurich.^[22]

2.2. THz TDS in Transmission Geometry

Figure 1a shows both variations of the THz TDS systems used in this work in transmission geometry. Here, a femtosecond laser with a pulse duration of 18 fs at full width at half maximum (FWHM), pulse energy of 5.0 nJ, repetition rate of 40 MHz, and an average power of 200 mW at the center wavelength of 1560 nm is used. The incoming laser beam is first split into the pump and the probe beam at the beam splitter (BS). The pump beam passes the optical modulator operating at 50 kHz and a stepper motor-based optical delay line to the THz generation (DAST or DSTMS) crystal. The lens in front of the generation crystal is used to adjust the pump-beam size. Two off-axis ellipsoidal mirrors reflect and refocus the generated THz waves through infrared filter(s) and the sample compartment to the detection crystal. The probe optical beam is directed through a small hole in the second ellipsoidal mirror and hits the detection crystal (DAST or DSTMS) at the same position as the THz waves. After the detection crystal, the probe beam hits the detection electronics where the photodetector detects the signal proportional to the THz electric field by the THz-induced lensing (TIL) principle.^[23] The principle is based on the detection of the focusing and defocusing of the probe beam in the presence of the THz electric field, which modifies the refractive index of the detection DAST or DSTMS crystal through the linear electro-optic (Pockels) effect, as described in more detail in a study by Schneider et al.^[23] A lock-in amplifier operating at the modulation frequency of 50 kHz is used for low-noise signal acquisition. In another variation of the THz TDS system in transmission geometry, a different type of the 1560 nm fiber-based femtosecond laser with an FWHM pulse duration of 38 fs, pulse energy of 1.9 nJ, repetition rate of 100 MHz, and average optical power 190 mW is used. Moreover, a custom-built voice-coil delay line with 10 nm incremental encoder resolution and on-the-fly data

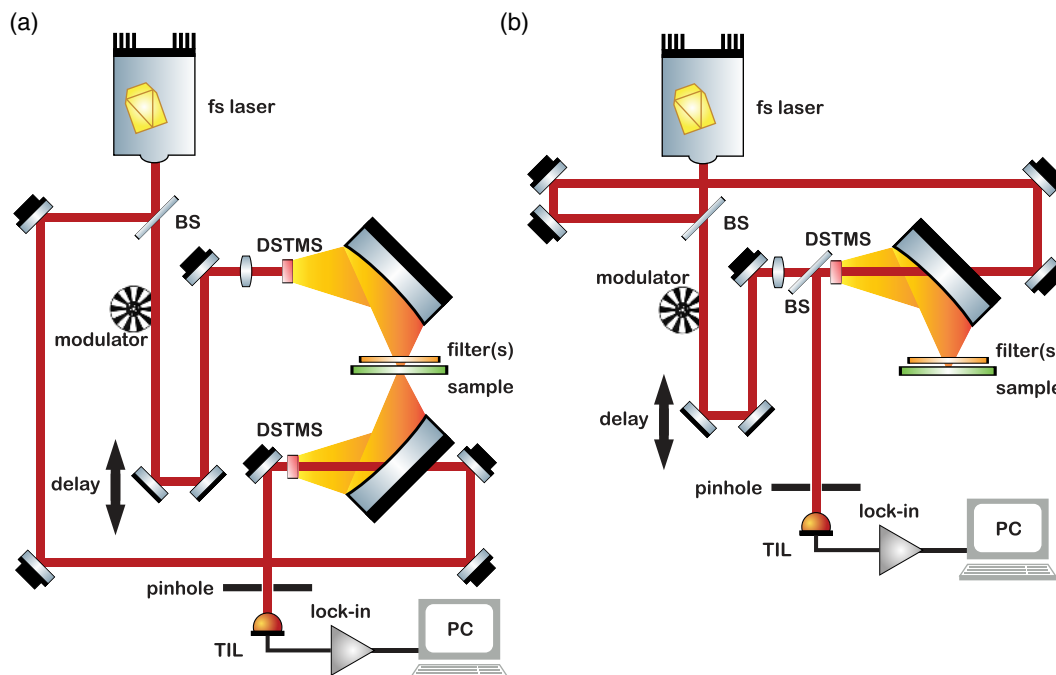


Figure 1. a) Schematics of the THz TDS setup in transmission geometry where a DSTMS crystal is used for both the generation and detection of the THz waves. The optical beam is split at the BS into the pump and the probe beam. The pump beam is delayed at the delay line and hits the generation DSTMS crystal where the THz waves are emitted in the same direction. The generated THz wave travels through an IR filter to the sample compartment and further to the detector DSTMS crystal where it overlaps with the probe beam. The THz signal is coherently detected by the TIL electro-optic principle using a photodetector and low-noise electronics with a lock-in operating at the modulation frequency of 50 kHz. The same setup is used in case of the DAST crystal. In b) normal-incidence reflection geometry, a similar approach is used. Here, a single organic crystal is used for both THz generation and detection.

acquisition was used, enabling a scan rate up to four traces per second and a 640 ps long delay between the THz pulse and the probe optical pulse.

The details of the used optical and the THz beam size and the ellipsoidal mirror parameters are given in Section 3.3, discussing the optimal geometry factors for ultra-broadband THz wave generation and detection in organic NLO crystals.

2.3. THz TDS in Reflection Geometry

In case of reflection geometry, the same 18 fs, 5.0 nJ, 40 MHz laser as in the transmission geometry described in Section 2.2 is used for the pump and the probe beam. The schematics of the reflection geometry setup is shown in Figure 1b. After the optical BS, the pump beam is delayed at the stepper motor-based optical delay line before it hits the DSTMS crystal and generates THz waves. The same off-axis ellipsoidal mirror as used in transmission focuses THz waves through the infrared filter to the sample or the reference flat mirror. The THz waves are reflected back from the sample surface under the normal-incidence geometry back to the DSTMS crystal that acts now as a THz wave detector. The probe beam goes through a small hole in the ellipsoidal mirror and hits the DSTMS crystal, where it overlaps with the THz waves reflected from the sample. A BS before the organic crystal reflects the probe beam into detection electronics, where, like in the transmission geometry, the TIL principle is used.

3. Terahertz Bandwidth Limitations and Theoretical THz Spectra

In this section we discuss the various parameters of our THz TDS system that limit the final bandwidth. These include the pulse width of the pump femtosecond laser pulses, THz phonon and vibrational modes of the organic crystals used for THz generation and detection, and the propagation losses due to specific THz and optical components in the system. We use a theoretical model for THz wave generation and detection to evaluate the expected THz spectrum and compare it with the measured THz spectrum. Our aim is to determine the optimal experimental conditions, which finally enable us to generate and coherently detect THz radiation in the extended THz range up to 20 THz and beyond at a high dynamic range. The whole process of THz generation, detection, and propagation has been previously modeled in a narrow THz range up to about 2.5 THz for standard inorganic ZnTe crystals.^[24,25] We here use models that have shown very good correspondence with experiments for organic NLO crystals derived by Schneider et al.^[4,26] We also consider other geometrical parameters during the THz beam propagation that are in particular relevant at higher THz frequencies f . To model the NLO conversion of pump optical pulses to broadband THz pulses for optical rectification, we use an analytical solution of the nonlinear wave equation in a non-depleted pump approximation. This approximation neglects cascaded NLO

effects, which is in our case justified by the relatively low pump pulse energy in the nJ range. In the plane-wave approximation, the THz electric field $E_{\text{THz}}(\omega, \lambda)$ generated in a material with a second-order NLO susceptibility $\chi^{(2)}$ at the THz angular frequency $\omega = 2\pi f$, pumped by an optical pulse at the central wavelength λ , is in this model expressed as^[4,26]

$$E_{\text{THz,plane}}(\omega, \lambda) = \frac{\mu_0 \chi^{(2)} \omega I(\omega)}{(n_{\text{THz}} + n_g + i \frac{\epsilon}{\omega} (\alpha_{\text{THz}}/2 + \alpha)) n} \cdot G(\omega) L \quad (1)$$

where

$$G(\omega) = \frac{e^{i(\frac{\omega}{c} n_{\text{THz}} + i \alpha_{\text{THz}}/2) L} - e^{i(\frac{\omega}{c} n_g + i \alpha) L}}{\frac{\omega}{c} (n_{\text{THz}} - n_g) L + i (\alpha_{\text{THz}}/2 - \alpha) L} \quad (2)$$

with $I(\omega)$ the Fourier transform of the pump optical pulse intensity $I(t)$, L the thickness of the NLO material, c the speed of light in vacuum, and μ_0 the magnetic constant. We consider the following material parameters in the optical and the THz range with the corresponding dispersion, including the phonon/vibrational absorption modes and the accompanying dispersion: the refractive index n_{THz} and the absorption coefficient α_{THz} at the THz angular frequency ω , as well as the optical refractive index n , the optical group index n_g , and the absorption coefficient α at the optical wavelength λ . The second-order NLO susceptibility for THz wave generation using optical rectification $\chi^{(2)}$ is related to the electro-optic coefficient r as $\chi^{(2)} = n^4 r/2$. We can assume this coefficient constant over the whole generated THz range because of the relatively low dispersion of our organic materials.^[6,27] We also use the optimal DAST and DSTMS crystal orientation, with the pump optical beam and the generated THz beam both polarized along the polar axis x_1 , allowing to use the largest electro-optic coefficient $r = r_{111} \approx 50 \text{ pm V}^{-1}$. We also consider all refractive indices/absorption coefficients along the x_1 axis of the otherwise strongly anisotropic crystals. The refractive indices and the absorption coefficients for DAST and DSTMS both in the optical and in the THz range are considered like the ones reported in the study by Jazbinsek et al.^[7] and the corresponding dielectric functions are given in Supporting Information. In the model represented with Equation (1) and (2) we also neglect the possible contribution of pulse broadening due to group velocity dispersion (GVD) in the generation and detection crystals, which may in addition modify the efficiency^[28] and in our case the bandwidth. Based on available material parameters, the GVD of DAST and DSTMS at 1560 nm is about $1000 \text{ fs}^2 \text{ mm}^{-1}$ (see Supporting Information), which leads to a broadening of an 18 fs transform-limited pulse to about 80 fs in a 0.5 mm crystal and about 110 fs in a 0.7 mm crystal, whereas for a 38 fs pulse, the broadening is less significant (up to about 53 fs in a 0.5 mm crystal). However, as we experimentally do not observe a remarkable difference in the performance of crystals of thickness in the 0.5–0.7 mm range, we neglect the effect of GVD in this work to keep the model as simple as possible.

3.1. Pump Pulse Duration

The first parameter limiting the final bandwidth is the pulse duration of the pump beam. We consider here transform-limited Gaussian pump pulses of the form $I(t) = I_0 e^{-t^2/(2\tau^2)}$, where

$\tau = \frac{\text{FWHM}}{\sqrt{8 \log(2)}} = \text{FWHM}/2.355$ and FWHM is the full width at half maximum duration of the pulse intensity. The Fourier transform of the pump optical pulse intensity is given by $I(\omega) = \sqrt{2\pi\tau} I_0 A(\omega)$, where $A(\omega)$ is the normalized Fourier spectrum $A(\omega) = \exp(-\tau^2 \omega^2/2)$. **Figure 2** shows the bandwidth limitation of the generated THz amplitude due to pulse duration, i.e., the frequency-dependent spectral factor $A(\omega)$. Note that due to GVD in the optical components and the organic crystals (see Section 3), the curve for the shortest pulse length of 18 fs will be effectively shifted to curves with a larger pulse duration. Nevertheless, for both of our experimental pulse durations of FWHM = 18 fs and 38 fs, we can expect to generate THz frequencies of up to 20 THz or in the case of FWHM = 18 fs above 20 THz without considering other possible limitations in the system, as discussed later.

3.2. Phase Matching and Absorption

The second important parameter is the amplitude response function $G(\omega)$ given by Equation (2), which strongly depends on the material parameters of the generator crystal and is in particular

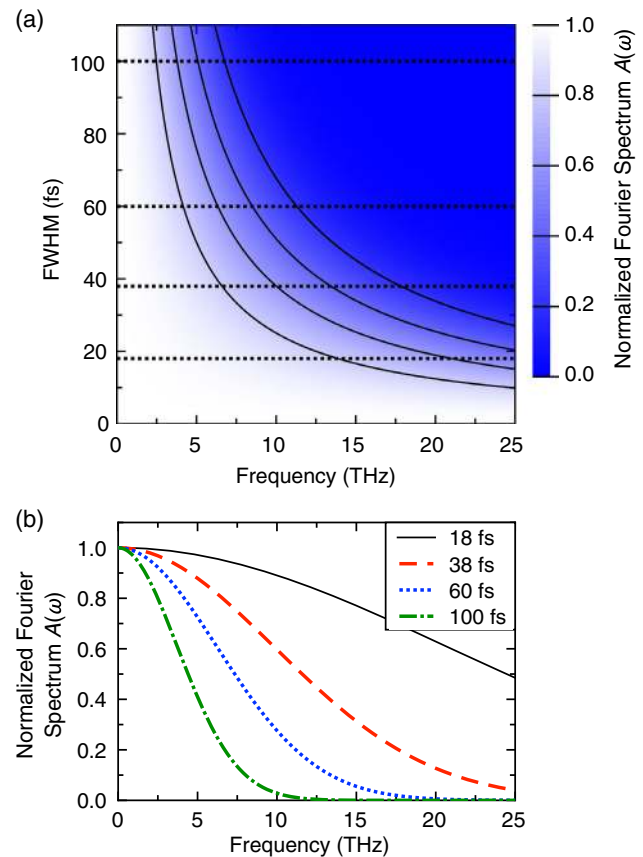


Figure 2. Normalized Fourier spectrum $A(\omega)$ of the pump optical beam: a) as a function of FWHM pulse duration; b) for pulse durations of 18 and 38 fs as in our experimental setup and for 60 and 100 fs (i.e., along the dotted horizontal lines of (a)). To reach the spectral width of 20 THz, pump-pulse duration below 40 fs is essential.

very sensitive to the phase-matching condition. The phase matching in case of THz generation by optical rectification is often referred to as velocity matching, as it basically requires a good matching between the phase velocity of the THz pulse and the group velocity of the pump optical pulse, i.e., $n_{\text{THz}} \approx n_g$.^[27] The amplitude response function $G(\omega)$ here is defined equivalently as the frequency response function introduced in a study by Wu et al.^[29] for inorganic crystals, but it additionally considers the material absorption for both the optical and the THz frequencies. For simplicity, the usual Fresnel coefficients are not included here, because they are different for the THz generation and the THz detection case and they also affect the overall spectral shape only marginally compared with $G(\omega)$. For perfect phase matching and negligible absorption, the amplitude response function $|G(\omega)| = 1$; otherwise, the amplitude of $|G(\omega)|$ determines the reduction factor due to the general non-perfectly matched case and due to the absorption of the generation material. The response function $|G(\omega)|$ strongly depends on the THz frequency, pump wavelength, as well as the material thickness. **Figure 3a** shows $|G(\omega)|$ as a function of the THz frequency $f = \omega/(2\pi)$ and thickness L for DSTMS and **Figure 3b** shows the spectra for selected thicknesses L , including the corresponding spectra for DAST, all considering a 1560 nm pump wavelength. Note that we could evaluate the frequency

dependence only up to 12 THz for DAST and DSTMS, which is the range of available THz refractive indices and absorption coefficients for these materials.^[7]

As $G(\omega)$ is independent of the pump pulse duration, it basically defines the spectrum achievable for ultra-short pump pulses (< 20 fs for the THz range of up to about 20 THz). Due to material absorption and limited coherence length, this frequency response function in general decreases with the overall crystal thickness L . However, as the generated field is in addition proportional to the thickness (see Equation (1)), a careful choice of the crystal length is needed to obtain the optimal THz field. **Figure 3c,d** shows the finally relevant figure, the product $|G(\omega)|L$, also known as the effective generation length,^[4] as a function of frequency and thickness. **Figure 3c** shows that for the crystal thickness range between 0.4 and 0.8 mm, which is also the range of the thicknesses we use in our experimental setup, the effective generation length is in the optimal range and only minor differences can be observed. Comparing DAST and DSTMS in **Figure 3b,d**, we can observe that the potential spectrum is smoother for DSTMS compared with DAST, which is due to the lower absorption of both phonon and vibrational mode resonances in DSTMS. DSTMS is therefore preferred based on our model and the available data on the optical and the THz properties.

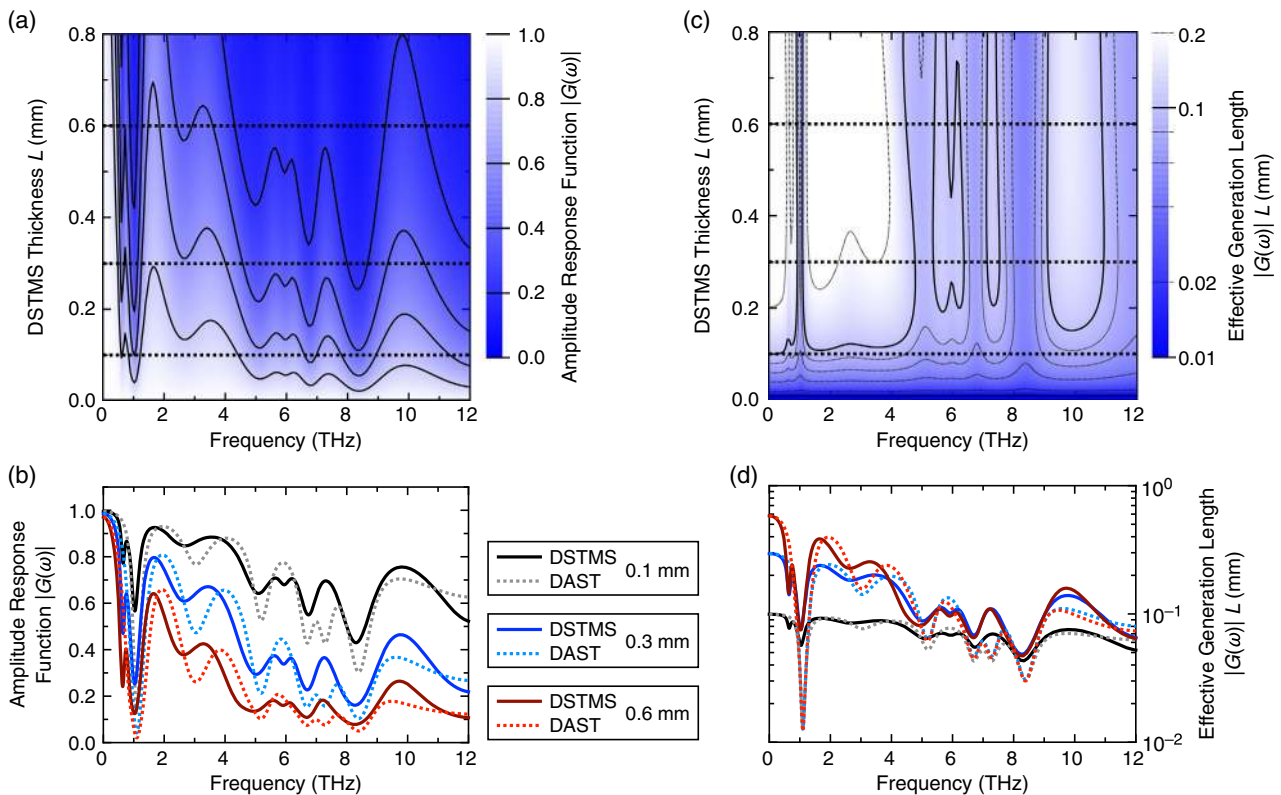


Figure 3. Influence of the optical and the THz properties of the generation material, i.e., phase matching and absorption, on the spectral characteristics of the generated THz pulse: a,b) The amplitude response function $|G(\omega)|$ according to Equation (2) and c,d) the effective generation length $|G(\omega)|L$ as a function of THz frequency and DSTMS generation crystal thickness L (a and c). (b) and (d) show spectra at selected crystal thicknesses L along the dotted horizontal lines of (a) and (c) and include in addition the corresponding curves for DAST. Although $|G(\omega)|$ decreases with the thickness due to in general nonperfect phase matching (a and b), the optimum crystal thickness is from about 0.4 mm to 0.8 mm (c and d). All curves are calculated for the pump wavelength of 1560 nm.

3.3. Geometric Factors

To achieve the highest possible conversion and detection efficiency, optimization of the pump-beam focusing and the THz optics is necessary. We are using relatively low average powers and very low pulse energies; we therefore do not need to consider the much higher limits due to the damage threshold in organic crystals. Following Equation (1), the generated THz field is proportional to the Fourier transform of the intensity $I(\omega)$, which is again proportional to τI_0 , as discussed earlier. The peak intensity I_0 is related to the peak power P_0 as $I_0 = P_0 / (\frac{1}{2}\pi w_{\text{opt}}^2)$, where w_{opt} is the pump-beam radius, i.e., half diameter at $1/e^2$ intensity. Combining these factors, it is easy to see that the generated THz field E_{THz} is directly proportional to the pump-beam fluence, i.e., $E_p / (\frac{1}{2}\pi w_{\text{opt}}^2)$, which increases with the pulse pump energy E_p (proportional to τP_0) and focusing, i.e., with smaller beam size w_{opt} . However, as discussed later, decreasing the pump-beam size increases the diffraction losses in THz generation. Also, THz propagation losses depend on the geometry of the setup and the size of optical components. Therefore, a compromise is needed for the pump-beam diameter to optimize the THz spectrum to be detected.

In our case, the pump beam is slightly focused with the beam radius of about $w_{\text{opt}} = (0.36 \pm 0.05)$ mm, which

reduces the generated THz electric field due to diffraction by a factor of r_w

$$r_w = \frac{\text{arcsinh}(x)}{x}; \quad x = \frac{4cL}{\omega w_{\text{opt}}^2} \quad (3)$$

The diffraction factor r_w becomes relevant for THz frequencies below 1 THz for crystal thicknesses of 0.2 mm and above. Examples for the reduction factor are shown in Figure 4a. As we use relatively thick crystals to increase the generation efficiency (thickness L in the range of 0.5–0.8 mm), we partially decrease the efficiency in the lower-frequency part below 1 THz compared with the case of a plane-wave pump beam, but the reduction in our targeted frequency range is not large, e.g., the factor r_w for a 0.7 mm-thick crystal and $w_{\text{opt}} = 0.36$ mm is still above 0.85 at 1 THz. The reduction becomes strong for tighter focusing (see Figure 4a for $w_{\text{opt}} = 0.10$ mm), whereas for very thin crystals, diffraction is less important (see Equation (3)).

Another factor related to the beam size is due to the losses at the mirrors used to steer the THz beam. This includes both the mirror size and the size of the hole in the mirror, which is often (also in our experimental configuration) used to direct the probe beam to the detection crystal collinear with the pump beam. In a

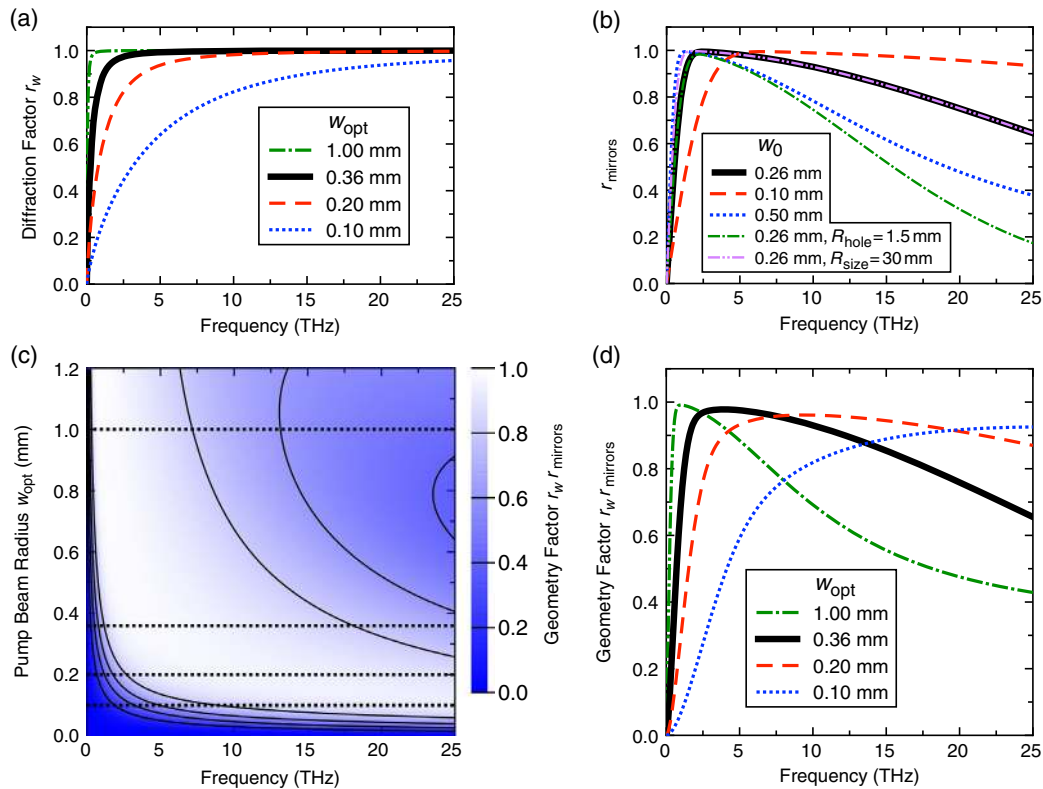


Figure 4. Geometry factors influencing the THz spectrum: a) Diffraction factor r_w (Equation 3) considering the diffraction of the THz field within the generation crystal for different values of the pump-beam radius w_{opt} at the crystal, considering a crystal length of $L = 0.7$ mm. b) THz amplitude reflection r_{mirrors} (Equation 4) at the mirrors steering and focusing the THz beam for different values of the THz beam waist w_0 and considering a focal length $f_M = 75$ mm, mirror radius $R_{\text{size}} = 20$ mm, and mirror hole radius $R_{\text{hole}} = 0.75$ mm (unless explicitly labeled). c) The influence of both geometry factors $r_w r_{\text{mirrors}}$ as a function of frequency and the pump-beam radius w_{opt} , considering $L = 0.7$ mm, $f_M = 75$ mm, $R_{\text{size}} = 20$ mm, and $R_{\text{hole}} = 0.75$ mm. d) Geometry factor $r_w r_{\text{mirrors}}$ for different values of w_{opt} along the dotted horizontal lines of (c). The thick black solid curve in (a), (b), and (d) corresponds to our experimental conditions.

study by Shalaby et al.,^[8] it is estimated that the hole in the mirror reduced the detected THz beam by a constant factor of about 0.6 over the whole spectral range. We however show that the hole in the mirror affects mostly higher THz frequencies. To evaluate the reduction due to the mirror, we consider a Gaussian beam shape of the THz beam with a beam waist of $w_0 = w_{\text{opt}}/\sqrt{2} \approx 0.26$ mm, where the factor of $\sqrt{2}$ is due to the fact that the generated THz field is proportional to the intensity of the pump at the position of the crystal $I(r) = I_0 \exp(-2r^2/w_{\text{opt}}^2)$ and therefore the generated THz power to $I^2(r)$. The THz beam size at the mirror (half diameter at $1/e^2$ THz intensity) is then $w(f_M) = w_0 \sqrt{1 + f_M^2/z_R^2} \approx w_0 f_M/z_R$, where f_M is the focal length of the mirror and $z_R = \pi w_0^2 f/c$ is the frequency-dependent Rayleigh range, i.e., larger the THz frequency f , smaller the THz beam size at the mirror $w(f_M)$. The THz amplitude reflection from the mirror (or both mirrors, if they are of the same size) can be therefore calculated as

$$r_{\text{mirrors}} = \left(\exp\left(-\frac{2R_{\text{hole}}^2}{w^2(f_M)}\right) - \exp\left(-\frac{2R_{\text{size}}^2}{w^2(f_M)}\right) \right)^{1/2} \quad (4)$$

where R_{size} and R_{hole} is the radius of the mirror and the radius of the hole in the mirror, respectively. Figure 4b shows the frequency dependence of r_{mirrors} considering all THz mirrors in the system of the same size and the focal length of $f_M = 75$ mm, which is an often-used focal length and is also used in our system. We can see that for our experimental parameters ($R_{\text{size}} = 20$ mm and $R_{\text{hole}} = 0.75$ mm, $w_0 \approx 0.26$ mm) we can well cover the whole spectral range from 0.1 to 20 THz, whereas a considerable reduction at higher frequencies occurs for a bigger hole size or for a larger THz beam waist. The increase in the mirror diameter from 20 mm to 30 mm in our case however only slightly increases this factor at frequencies below 3 THz.

Figure 4c,d shows the combined geometry factor $r_w r_{\text{mirrors}}$ as a function of frequency and pump-beam size w_{opt} . One can see that for a certain range of pump-beam sizes we can propagate both lower and higher THz frequencies. For tight focusing, we cut considerably the low-frequency part, whereas for the larger beam size, the higher frequencies are cut. The optimal beam size depends on the generation crystal length and the parameters of the THz mirrors (focal length, size, and the size of the hole). Note that the high-frequency part of the spectrum will not be reduced in the same way in case a different optical element (such as a dichroic mirror) is used to overlap the THz and the probe optical beam in the detection crystal; in this case, the THz transmission properties of the dichroic mirror should be considered instead.

3.4. Electro-Optical Detection

For electro-optically based THz wave detection, we use crystals of the same type as used for THz wave generation. Like this, we profit from both the high bandwidth and the high electro-optic coefficient of organic crystals compared with usually used semiconductors such as ZnTe or GaP, which are additionally not phase matchable at 1560 nm.^[29,30] As organic electro-optic crystals are strongly birefringent (see Supporting Information), we cannot use the standard electro-optic sampling detection as used for semiconductors.^[29,31] This is because the orthogonal field

components will become decoherent after passing the detection crystal (with a delay time in the order of 1 ps) with a large phase shift ($> 100 \cdot (2\pi)$) that cannot be compensated by a variable waveplate as for materials with a smaller birefringence.^[32] Instead we use the electro-optic lensing effect, which also achieves a high electro-optic sampling sensitivity.^[23] We confirmed experimentally that the detection is in our case perfectly linear and the nonlinear THz effects occurring at very strong THz fields^[33,34] do not play a role yet. For electro-optic detection, the phase matching, i.e., matching between the phase velocity of the THz pulse and the group velocity of the probe optical pulse, is as important as for the THz wave generation part. The phase-matching characteristics have an equivalent dependence on the probe pulse duration and material parameters, as for the THz wave generation by optical rectification. The induced phase shift of the probe beam $\Delta\phi(\omega)$ due to the presence of the THz field $E_{\text{THz}}(\omega)$ can be expressed as

$$\Delta\phi(\omega) = \frac{2\pi}{\lambda} \cdot \frac{n^3 r}{2} \cdot G_{\text{det}}(\omega) \cdot L_{\text{det}} \cdot A(\omega) \cdot E_{\text{THz}}(\omega) \quad (5)$$

and therefore scales with the detection crystal thickness L_{det} , the normalized Fourier transform of the probe optical pulse $A(\omega)$, which is in our case identical to that of the pump pulse, and the amplitude response function $G_{\text{det}}(\omega)$, which can be calculated using the same Equation (2) valid for the THz wave generation, by considering the detection crystal thickness L_{det} instead of the generation crystal thickness L .

The final signal will be proportional to

$$S_{\text{EO}}(\omega) \propto t_{\text{filters}} \cdot r_{\text{mirrors}} \cdot r_w(\omega, L) G(\omega, L) G(\omega, L_{\text{det}}) A(\omega)^2 \cdot \omega \cdot L \cdot L_{\text{det}} \quad (6)$$

where we only explicitly wrote the parameters with the strongest THz frequency dependence, important for the bandwidth limitation of the THz generation and detection process, as well as the generator and detector thickness dependence. Note that for the evaluation of the signal we may in addition consider the usual Fresnel reflection factors for the optical and the THz beams. However, for the frequency-dependence/bandwidth limitations, these factors are less important. Another important factor in Equation (6), t_{filters} , considers amplitude transmission through various filters that may be used in the beam path, which are mostly needed to filter out the pump laser beam to not disturb the detection. There may be many cases found in literature, where the THz spectrum of organic crystals is considerably limited due to the bandwidth of the filter used (e.g., a thicker piece of Teflon). Note that the transmission function through various (combined) filters may be in addition quite complex.^[35] In our case, we use (alone or in combination) different filters: 1) a 0.5 mm-thick Ge wafer, with an amplitude transmission of about 60% and an almost flat spectral transmission up to above 20 THz, except for some minor absorption features in the 10–15 THz range;^[36] 2) a 20 THz low-pass filter with an amplitude transmission varying between about 0.90 and 0.98 in the whole range; and 3) a piece of Styrofoam that limits the bandwidth up to about 15 THz. The choice of the filter may considerably limit the bandwidth of the THz spectrum and may add multiple THz

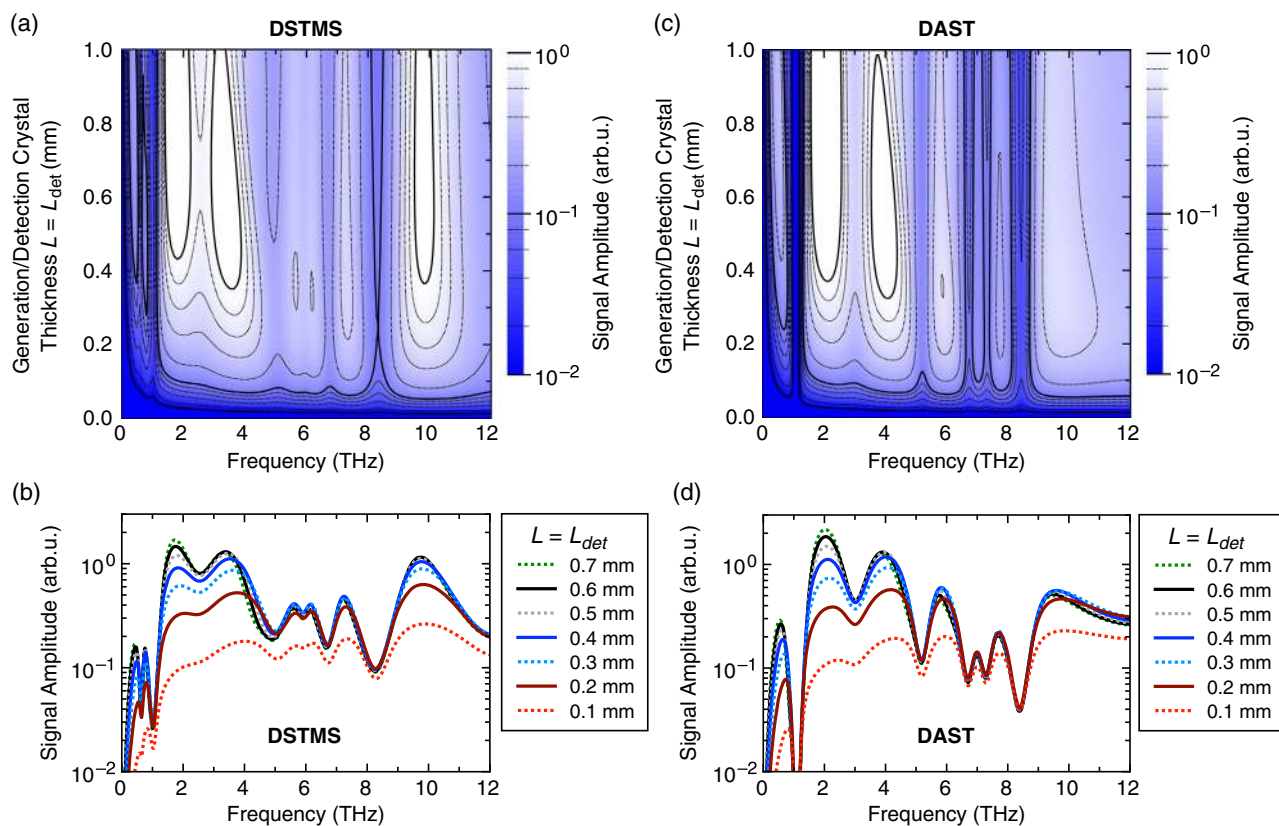


Figure 5. The theoretical THz signal amplitude S_{EO} according to Equation (6) for an optimal filter transmission $t_{\text{filters}} = 1$ as a function of frequency and crystal thickness L , considering that the detection crystal has the same length $L_{\text{det}} = L$ and a,b) DSTMS or c,d) DAST as generators/detectors. (b) and (d) show selected spectra of Figure (a) and (c), respectively. For all curves we consider our experimental parameters, i.e., the pump wavelength of 1560 nm, pump/probe pulse duration of FWHM = 18 fs, pump-beam radius $\omega_{\text{opt}} = 0.36$ mm, and THz mirror(s) with the following parameters: $f_M = 75$ mm, $R_{\text{size}} = 20$ mm, and $R_{\text{hole}} = 0.75$ mm.

reflections in case of longer time scans, so the optimal choice of the filter depends on the final application.

Figure 5 shows the expected signal amplitude as a function of DAST or DSTMS crystal thickness and frequency up to 12 THz (range of available material parameters). As the generation and detection crystal thicknesses appear symmetrically in Equation (6), we consider $L = L_{\text{det}}$ for this illustration. For thin crystals (≈ 0.1 mm), the overall spectral shape is very smooth, but the amplitude is one order of magnitude smaller than possible with optimal crystal thicknesses of above 0.5 mm. We can observe that the crystal thickness above 0.5 mm does not play a considerable role anymore and can only improve the signal at certain THz frequencies with perfect phase matching. Therefore, we consider crystals in the range of 0.5–0.8 mm as optimal for our application. For crystals of above 0.5 mm thickness, the bulk crystal quality and the quality of the surface polishing are more important than the crystal thickness. The results and conclusions are very similar for DSTMS and DAST. We see here again that the signal reduction at phonon and vibrational mode resonances is more pronounced for DAST at most of the peaks, not only for the phonon mode at about 1 THz as previously observed.^[37] This advantage of DSTMS over DAST is also confirmed experimentally, as discussed in the following section.

4. Measurement Results

4.1. Transmission Geometry of the THz TDS System

Figure 6a shows the THz time-domain signal acquired in the transmission geometry using the 18 fs laser. Here, each THz TDS system uses either a pair of DAST or a pair of DSTMS organic crystals for THz generation and detection. The thickness of DAST was 0.63 mm for THz generation and 0.54 mm for THz detection. In case of DSTMS we used 0.68 mm for THz generation and 0.73 mm for THz detection. The time-domain signals were acquired in dry air environment with less than 7% relative humidity (RH), signal acquisition length of 8.5 ps, and averaging time of 1 s per point. In total, 144 points ps^{-1} were recorded, thus corresponding to a temporal resolution of ≈ 6.9 fs and a band limit (Nyquist frequency) of 72 THz. One can notice already from the few-cycle time-domain signals that the time difference between adjacent peaks is in the order of tens of femtoseconds, therefore suggesting that high-frequency components are present in the signal. Both combinations of crystals, DAST/DAST or DSTMS/DSTMS, gave similar results for the amplitude and beam shape, which are in agreement with the similar electro-optic coefficient of both organic NLO crystals, their thickness,

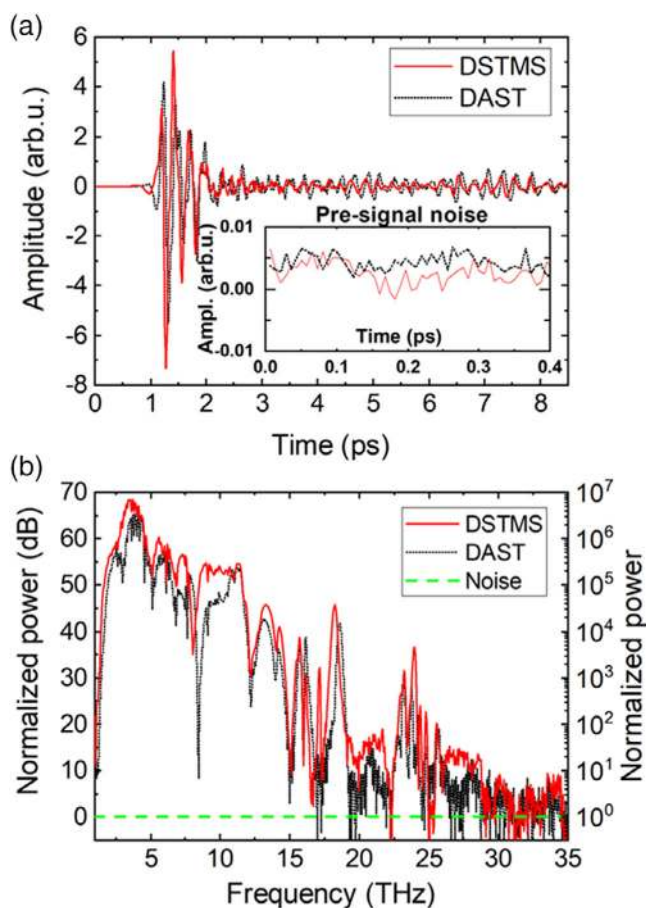


Figure 6. a) THz time-domain signal acquired with a pair of DAST and DSTMS crystals under the same experimental conditions with the 18 fs laser source (40 MHz repetition rate, 5.0 nJ pulse energy). The inset shows the presignal noise for both THz TDS systems in transmission geometry with different crystal pairs. b) The corresponding spectrum of both time-domain signals normalized to the noise floor (green dotted line).

analogous structure, similar optical properties, and same experimental conditions. In Figure 6b, a normalized spectrum of both measured time-domain signals is shown in the frequency range from 1 to 35 THz. Below 1 THz both spectra have low SNRs due to absorptions in the germanium infrared (IR) filter used here and phonon absorptions in the organic crystals. This agrees with the modeled prediction in Figure 5b,d. The phonon absorptions are also present in the regions from 7–9 THz to 15–20 THz. The DAST/DAST combination in particular has a high absorption at frequencies around 8 THz, whereas with the DSTMS/DSTMS combination, the absorption is shifted slightly to lower frequencies due to the different molecular structure of the crystals. This vibrational mode is due to π -bridge bending of the cation NLO chromophore according to periodic density functional theory calculations for DAST.^[38] One can note that practically all absorption dips of the DSTMS pair are lower than the dips with the DAST pair, in accordance with the corresponding theoretical amplitude response function shown in Figure 3b. Both crystal combinations exhibit an almost gap-free THz spectrum with a

high SNR up to 15 THz. We were able to reach an SNR of around 70 dB in the transmission geometry with both crystal combinations and the 18 fs laser, which to our knowledge is record-high SNR for the electro-optic detection using organic NLO crystals. Due to the advantages of detecting THz signals using organic electro-optic crystals instead of standard inorganic crystals (e.g., ZnTe or GaP), a high SNR is also achieved at frequencies beyond the usual limit of about 6 THz, e.g., larger than 50 dB at 10 THz. Up to 15 THz the frequency spectrum of both crystal pair configurations is similar, except for the details of the vibrational-induced dips, which agree well with the calculated spectrum up to 12 THz (Figure 5b,d). Note that due to the complexity and the limited accuracy of the available material parameters, the details of the theoretical and the experimental spectrum can still differ. At 15 THz, there is a relatively strong absorption in both crystals. The frequency peaks around 16 THz are well expressed with a slightly higher amplitude in the case of the DAST pair. Of interest is the frequency peak at 17 THz that appears only with the DSTMS combination. The peak around 18.5 THz has almost the same amplitude in both combinations. However the peak for DSTMS is shifted by 0.2 THz toward lower frequencies. A gap until 23 THz is present in both configurations due to phonon absorptions in the crystals. The spectrum above 25 THz is limited by pulse duration, geometry, and phase matching, as discussed in Section 3. Finally, above 30 THz the noise dominates. Comparing the spectral features at frequencies beyond 12 THz with the results of narrowband THz wave generation by another NLO process of difference frequency generation in DAST^[39] and DSTMS^[40] shows a very good agreement, including the existence of the peak at around 17 THz for DSTMS only. This confirms that the high-frequency components in the spectrum are real and are not due to eventual high-frequency artifacts that may appear in some THz TDS systems due to sampling errors.^[41]

4.2. Reflection Geometry of the THz TDS System

In Figure 7, the THz time-domain signal and the corresponding frequency spectrum in the reflection geometry are shown, using the 18 fs laser source and a 0.68 mm-thick DSTMS crystal. The time-domain signal was acquired under the same settings as in the transmission geometry, at a resolution of 144 points ps^{-1} , equaling the same temporal resolution of 6.9 fs with 1 s averaging time per point. The total acquisition length of the recorded signal was 9 ps. The signal was acquired in dry air environment at 7% RH. As with the transmission setup, the higher frequency components can be noticed already from the narrow oscillations in the few-cycle THz signal. This is thereafter confirmed in the normalized reflection spectrum where THz frequencies higher than 20 THz can be observed. One can note from the comparison of the reflection and transmission spectrum that the frequency features are very similar for both, as expected, when using the same generation/detection material, optics, and pump laser. The SNR in the reflection mode is ≈ 10 dB lower. This is attributed to an additional BS necessary for reflection geometry at normal incidence, which reduces the pump-beam fluence at the crystal and therefore the amplitude of the generated THz field, as well as the intensity of the probe beam, which may increase

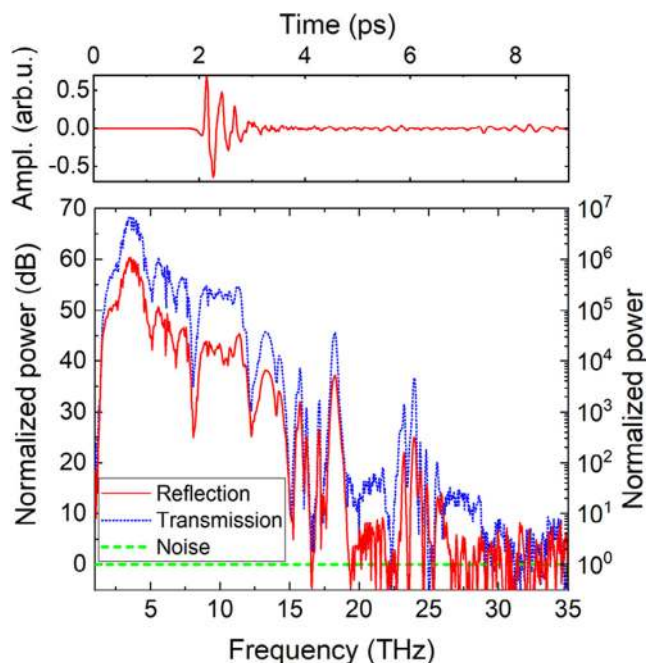


Figure 7. The measured THz time-domain signal in the reflection geometry (top) and the corresponding spectrum (bottom) obtained with the DSTMS crystal and the 18 fs laser source. For comparison, the spectrum in transmission geometry obtained with the same laser source and generation crystal from Figure 6 is presented; both spectra are normalized to the corresponding noise floor.

the relative noise level. The maximum SNR of 60 dB is achieved at 3.5 THz and is still above 40 dB at 10 THz.

4.3. THz TDS System with 38 fs Pump

The THz TDS system in transmission geometry discussed in this section is based on a different laser source with 38 fs pulse duration and a high repetition rate of 100 MHz as described in Section 2. Here, a similar optical setup is used and a 0.70 mm DSTMS crystal serves as a THz generator and a 0.76 mm-thick crystal as a THz detector. Moreover, a custom-built voice-coil-based optical delay line with on-the-fly data acquisition is used instead of the stepper motor. The THz time-domain signal shown in **Figure 8** was recorded over an acquisition period of 12.5 ps and averaged 2100 times. The acquisition speed was set to $300 \mu\text{m s}^{-1}$ and a triggering resolution to 300 nm intervals, which corresponds to a time resolution of 2 fs, in turn corresponding to the band limit (Nyquist frequency) of 250 THz. The obtained SNR was more than 80 dB, which is over 10 dB higher as the one obtained with the 18 fs laser source. This can be partially attributed to the averaging of the time-domain signal due to the longer total integration time of the acquired points. Up to about 19 THz the spectrum features are equivalent to the features obtained with the first THz TDS system shown in Figure 6. Above 20 THz the spectrum is suppressed, as expected, due to the longer pulse duration of the used laser (see Figure 2). This shows that even for the lower pulse

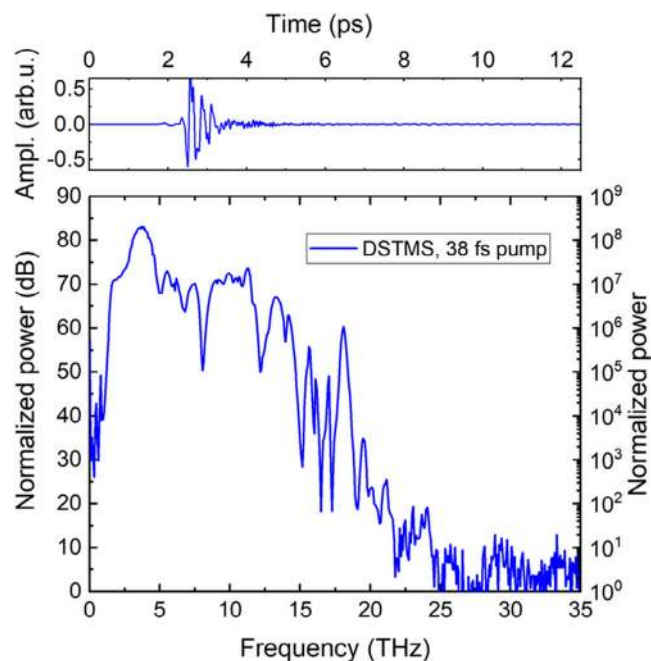


Figure 8. The measured THz time-domain signal in transmission geometry and the corresponding spectrum obtained with the 38 fs laser source (100 MHz repetition rate, 1.9 nJ pulse energy) and on-the-fly signal acquisition. The obtained SNR is above 80 dB at 4 THz and more than 70 dB at 10 THz and the frequency features are well expressed up to 20 THz. The spectrum was obtained by averaging the time-domain signal 2100 times.

energy available with this laser (1.9 nJ) compared with 5 nJ for the 18 fs laser), we can still obtain a very high SNR of the system in the 1–20 THz range by optimization of the optics and signal acquisition. The details of the high-frequency features (such as the sharp peak at 17 THz) correspond perfectly to those of the system based on the 18 fs laser and the stepper-motor delay line, which confirm that also in this system with the on-the-fly acquisition principle, high-frequency artifacts are not observed.

For improving the spectrum around and below the strong phonon resonance at 1 THz, which is already considerably improved for DSTMS compared with DAST (see Figure S2b, Supporting Information), as well as reduce the oscillations of the spectrum due to vibrational modes in DAST or DSTMS, other organic crystals being developed^[42–46] may lead to improved performance of such systems in the future. Inserting a conventional 1 mm-thick (110) ZnTe in its optimal orientation as the THz generator in the same THz setup (with DSTMS detector) results in a THz electric field amplitude of more than two orders of magnitude smaller, which is because of nonoptimal phase-matching conditions of ZnTe at 1560 nm pump wavelength, as well as a more than one order of magnitude smaller electro-optical figure of merit of ZnTe compared with DAST or DSTMS.^[7] Note that in none of the setups we observed any damage or degradation of the organic crystals used after several years of keeping the samples at normal room temperature (15–30 °C) and humidity conditions (30–60% RH) as well as after continuous operation/illumination of several days in the setups described.

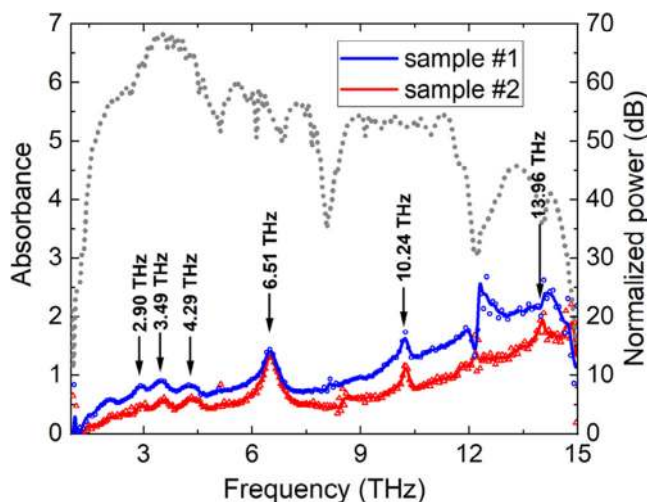


Figure 9. Absorbance of paracetamol (two different thicknesses) with the transmission geometry THz TDS system in the frequency range up to 15 THz. The background increase of the absorbance with the frequency is due to scattering. The dotted gray curve represents the normalized reference spectrum for this measurement (right scale), which limits the maximal measurable sample absorbance.

4.4. Validation Using Pharmaceutical Samples

The validation of the system was conducted using well-known pharmaceutical samples. We carried out spectroscopic measurements of paracetamol that has many frequency features up to 20 THz. Paracetamol has distinctive peaks at around 6.55, 10.20, 13.94, 15.12, and 15.56 THz according to measurements

using a conventional Fourier transform infrared spectrometer.^[47] Paracetamol tablets were ground, and a thin layer was then placed between two scotch tape layers with an excellent THz transmission. We were able to evaluate the absorbance in the frequency range up to 15 THz. Scattering from the grains limited the measurement above 15 THz. **Figure 9** shows the absorbance of two paracetamol samples. The red absorbance curve shows a sample with the thickness of about $(60 \pm 20) \mu\text{m}$ and the blue one shows a sample with the thickness of about $(90 \pm 30) \mu\text{m}$ (note that the thickness was not very regular across the sample). Note also the peaks between 2.90 and 4.29 THz which are not explicitly mentioned in the before-mentioned reference; however, they are clearly present in both samples. The artefacts around 8 and 12 THz are due to the limitations of the dynamic range at these frequencies, also due to increased scattering of the powdered samples, and therefore are not intrinsic spectral features of paracetamol.

4.5. High-Resolution Water Vapor Absorption

To evaluate the frequency accuracy of the newly developed THz TDS system, we compared the experimental and the theoretical THz absorption peaks of water vapor. The calculated absorbance at a resolution of 300 MHz is based on the HITRAN database of water vapor absorption data, which present the absorption cross section per molecule based on ab initio calculations.^[48] The absorbance was then calculated by considering the density of water molecules in humid air at room temperature and for an RH of 30%, at which our experiments were conducted, and the THz propagation length as 30 cm as in our experimental set-up. For the measurements, we used the same THz TDS system

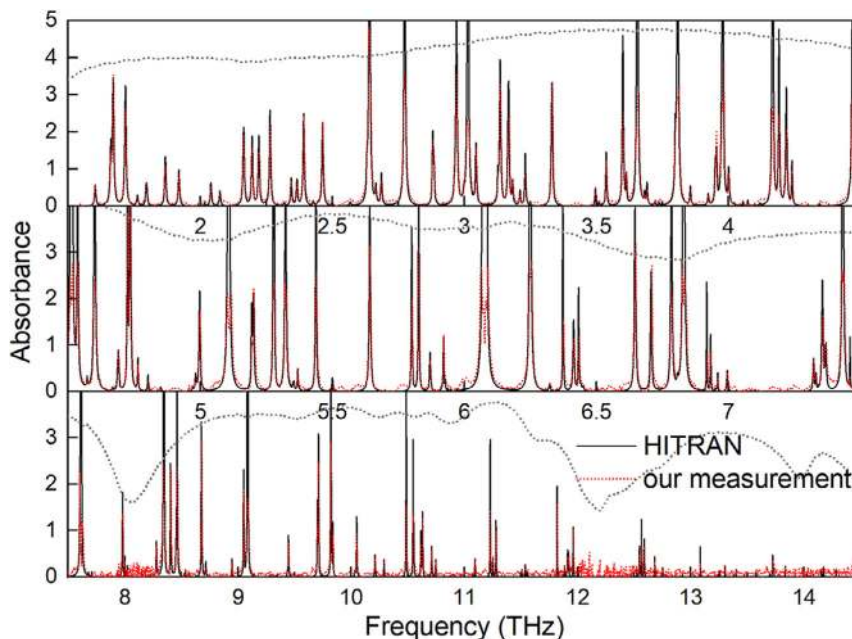


Figure 10. Validation of the THz TDS system in transmission geometry by measuring the water vapor absorption lines with the high resolution of 2.7 GHz (0.090 cm^{-1}) and comparing them with the results from the HITRAN database. The calculated relative frequency difference between the measured and the calculated absorption lines of the peaks is less than 0.05% over the whole spectral range. The dotted gray line represents the absorbance limit of this measurement.

described in Section 4.3. The acquisition speed was set to $30 \mu\text{m s}^{-1}$, with 300 nm triggering intervals and an acquisition length of 366 ps, corresponding to a spectral resolution of 2.7 GHz in frequency or a resolution of 0.090 cm^{-1} in spectroscopic wavenumber. Each time-domain measurement was averaged 50 times. The reference measurement was carried out in dry air with RH below 1% and otherwise with the same experimental conditions and acquisition parameters.

The comparison shown in **Figure 10** is depicted for the frequency interval 1.5–14.5 THz. In this range most of the features are present and the SNR of the system is high enough to have a clear distinction of water vapor absorption features, which are particularly strong in the 1.5–10 THz window and start to diminish for frequencies above 10 THz. The calculated relative difference between randomly selected measured and calculated absorption lines of the peaks is 0.044% at 1.86 THz, 0.026% at 5.20 THz, 0.034% at 10.05 THz, and 0.029% at 12.59 THz. This corresponds to a frequency difference of less than 5 GHz over the whole spectral range, comparable with the resolution of 2.7 GHz for this measurement. This shows a remarkable accuracy and proves that all the optimizations done within the new THz TDS system work correctly without the need for an additional calibration.

5. Conclusion

In this work we developed an ultra-broadband and high-dynamic-range THz TDS system based on organic NLO crystals used for both generation and detection of THz waves. The new THz TDS system covers the whole frequency range from 1 THz to more than 20 THz with a peak dynamic range of more than 80 dB. This surpasses the performance of all THz TDS systems based on photoconductive antennae. The system shows a very stable performance without any organic crystal degradation for the high-optical-quality DAST and DSTMS crystals used in this work. We theoretically analyzed and optimized various parameters that limit the final bandwidth. These include the pulse width of the pump femtosecond laser pulses, the THz phonon and vibrational modes of the organic crystals used for THz generation and detection, and propagation losses due to specific THz/optical components in the system. The measurement results show remarkable performance with a peak dynamic range of more than 80 dB for the THz TDS system in transmission geometry and ultra-broadband bandwidth exceeding 20 THz. Due to the detection advantage using organic electro-optic crystals and MHz repetition rates, a high SNR of more than 70 dB is also achieved at higher frequencies around 10 THz. A similar bandwidth is observed also for the system using normal-incidence reflection geometry with only about 10 dB lower signal to noise compared with the transmission geometry case. Future improvements are possible by developing optimized organic crystals with higher nonlinearity or weaker phonon and vibrational resonances. The performance of the system has been validated successfully by identifying specific high-frequency absorption features of pharmaceutical samples and by achieving a relative frequency difference of less than 0.05% between the measured and the reference HITRAN narrow absorption peaks of water vapor at a high experimental frequency resolution of 2.7 GHz (0.090 cm^{-1}).

Supporting Information

Supporting Information is available from the Wiley Online Library or from the author.

Acknowledgements

The authors thank Vincent Michel and Marcin Krajewski for technical help with the THz system development. The authors also thank Rainbow Photonics AG for discussions and for providing various equipment components and all organic NLO crystal samples for this study. This work was supported by the Swiss Innovation Agency (Innosuisse grant no. 19281.2 PFNM-NM), Swiss National Science Foundation (SNSF grant no. IZKSZZ_188194), and by Slovenian Research Agency research core funding (P1-0192).

Conflict of Interest

The authors declare no conflict of interest.

Keywords

DAST, DSTMS, organic crystals, reflections, spectroscopies, terahertz, transmissions

Received: October 15, 2020

Revised: December 10, 2020

Published online: February 17, 2021

- [1] S. S. Dhillon, M. S. Vitiello, E. H. Linfield, A. G. Davies, M. C. Hoffmann, J. Booske, C. Paoloni, M. Gensch, P. Weightman, G. P. Williams, E. Castro-Camus, D. R. S. Cumming, F. Simoens, I. Escorcia-Carranza, J. Grant, S. Lucyszyn, M. Kuwata-Gonokami, K. Konishi, M. Koch, C. A. Schmuttenmaer, T. L. Cocker, R. Huber, A. G. Markelz, Z. D. Taylor, V. P. Wallace, J. A. Zeitler, J. Sibik, T. M. Korter, B. Ellison, S. Rea, et al., *J. Phys. D: Appl. Phys.* **2017**, *50*, 043001.
- [2] X. C. Zhang, A. Shkurinov, Y. Zhang, *Nat. Photonics* **2017**, *11*, 16.
- [3] N. M. Burford, M. O. El-Shenawee, *Opt. Eng.* **2017**, *56*, 010901.
- [4] A. Schneider, M. Neis, M. Stillhart, B. Ruiz, R. U. A. Khan, P. Günter, *J. Opt. Soc. Am. B* **2006**, *23*, 1822.
- [5] P. U. Jepsen, D. G. Cooke, M. Koch, *Laser Photonics Rev.* **2011**, *5*, 124.
- [6] M. Jazbinsek, L. Mutter, P. Gunter, *IEEE J. Sel. Top. Quantum Electron.* **2008**, *14*, 1298.
- [7] M. Jazbinsek, U. Puc, A. Abina, A. Zidansek, *Appl. Sci.* **2019**, *9*, 882.
- [8] M. Shalaby, C. P. Hauri, *Nat. Commun.* **2015**, *6*, 5976.
- [9] X. Chai, X. Ropagnol, A. Ovchinnikov, O. Chefonov, A. Ushakov, C. M. Garcia-Rosas, E. Isgandarov, M. Agranat, T. Ozaki, A. Savel'ev, *Opt. Lett.* **2018**, *43*, 5463.
- [10] Y. Zhang, X. Zhang, S. Li, J. Gu, Y. Li, Z. Tian, C. Ouyang, M. He, J. Han, W. Zhang, *Sci. Rep.* **2016**, *6*, 26949.
- [11] P. J. Hale, J. Madeo, C. Chin, S. S. Dhillon, J. Mangeney, J. Tignon, K. M. Dani, *Opt. Express* **2014**, *22*, 26358.
- [12] S. Kono, M. Tani, K. Sakai, *IEE Proc. – Optoelectron.* **2002**, *149*, 105.
- [13] S. Kono, M. Tani, K. Sakai, *Appl. Phys. Lett.* **2001**, *79*, 898.
- [14] Y. Cai, I. Brener, J. Lopata, J. Wynn, L. Pfeiffer, J. B. Stark, Q. Wu, X. C. Zhang, J. F. Federici, *Appl. Phys. Lett.* **1998**, *73*, 444.
- [15] R. J. B. Dietz, B. Globisch, H. Roehle, D. Stanze, T. Göbel, M. Schell, *Opt. Express* **2014**, *22*, 19411.

- [16] H. A. Hafez, X. Chai, A. Ibrahim, S. Mondal, D. Férachou, X. Ropagnol, T. Ozaki, *J. Opt.* **2016**, *18*, 093004.
- [17] T. Seifert, S. Jaiswal, U. Martens, J. Hannegan, L. Braun, P. Maldonado, F. Freimuth, A. Kronenberg, J. Henrizi, I. Radu, E. Beaurepaire, Y. Mokrousov, P. M. Oppeneer, M. Jourdan, G. Jakob, D. Turchinovich, L. M. Hayden, M. Wolf, M. Münzenberg, M. Kläui, T. Kampfrath, *Nat. Photonics* **2016**, *10*, 483.
- [18] A. Singh, A. Pashkin, S. Winnerl, M. Welsch, C. Beckh, P. Sulzer, A. Leitenstorfer, M. Helm, H. Schneider, *Light Sci. Appl.* **2020**, *9*, 30.
- [19] Z. Yang, L. Mutter, M. Stillhart, B. Ruiz, S. Aravazhi, M. Jazbinsek, A. Schneider, V. Gramlich, P. Günter, *Adv. Funct. Mater.* **2007**, *17*, 2018.
- [20] S.-H. Lee, B.-J. Kang, J.-S. Kim, B.-W. Yoo, J.-H. Jeong, K.-H. Lee, M. Jazbinsek, J. W. Kim, H. Yun, J. Kim, Y. S. Lee, F. Rotermund, O.-P. Kwon, *Adv. Opt. Mater.* **2015**, *3*, 756.
- [21] L. Mutter, F. D. Brunner, Z. Yang, M. Jazbinšek, P. Günter, *J. Opt. Soc. Am. B* **2007**, *24*, 2556.
- [22] Rainbow Photonics AG – Terahertz Sources, Terahertz Spectroscopy, Terahertz Imaging, Organic Electro-Optic Crystals, Tunable Infrared Lasers, <http://www.rainbowphotonics.com/> (accessed: October 2020).
- [23] A. Schneider, I. Biaggio, P. Günter, *Appl. Phys. Lett.* **2004**, *84*, 2229.
- [24] J. Faure, J. Van Tilborg, R. A. Kaindl, W. P. Leemans, *Opt. Quantum Electron.* **2004**, *36*, 681.
- [25] A. Tomasino, A. Parisi, S. Stivala, P. Livreri, A. C. Cino, A. C. Busacca, M. Peccianti, R. Morandotti, *Sci. Rep.* **2013**, *3*, 3116.
- [26] A. Schneider, *Phys. Rev. A* **2010**, *82*, 033825.
- [27] L. R. Dalton, P. Günter, M. Jazbinsek, O.-P. Kwon, P. A. Sullivan, *Organic Electro-Optics and Photonics: Molecules, Polymers, and Crystals*, Cambridge University Press, Cambridge **2015**.
- [28] D. N. Erschens, D. Turchinovich, P. U. Jepsen, *J. Infrared Milli Terahz Waves* **2011**, *32*, 1371.
- [29] Q. Wu, X.-C. Zhang, *Appl. Phys. Lett.* **1997**, *70*, 1784.
- [30] A. Leitenstorfer, S. Hunsche, J. Shah, M. C. Nuss, W. H. Knox, *Appl. Phys. Lett.* **1999**, *74*, 1516.
- [31] P. C. M. Planken, H.-K. Nienhuys, H. J. Bakker, T. Wenckebach, *J. Opt. Soc. Am. B, JOSAB* **2001**, *18*, 313.
- [32] P. Y. Han, M. Tani, F. Pan, X.-C. Zhang, *Opt. Lett.* **2000**, *25*, 675.
- [33] Y. Shen, G. L. Carr, J. B. Murphy, T. Y. Tsang, X. Wang, X. Yang, *Phys. Rev. A* **2010**, *81*, 053835.
- [34] F. Giorgianni, U. Puc, M. Jazbinsek, T. Cea, M.-J. Koo, J.-H. Han, O.-P. Kwon, C. Vicario, *Opt. Lett.* **2019**, *44*, 4881.
- [35] K. J. Kaltenecker, E. J. R. Kelleher, B. Zhou, P. U. Jepsen, *J. Infrared Milli Terahz Waves* **2019**, *40*, 878.
- [36] A. Singh, A. Pashkin, S. Winnerl, M. Helm, H. Schneider, *ACS Photonics* **2018**, *5*, 2718.
- [37] M. Stillhart, A. Schneider, P. Günter, *J. Opt. Soc. Am. B* **2008**, *25*, 1914.
- [38] S. Saito, T. M. Inerbaev, H. Mizuseki, N. Igarashi, R. Note, Y. Kawazoe, *Chem. Phys. Lett.* **2006**, *432*, 157.
- [39] T. Notake, K. Nawata, H. Kawamata, T. Matsukawa, H. Minamide, *Opt. Mater. Express* **2012**, *2*, 119.
- [40] P. Liu, D. Xu, Y. Li, X. Zhang, Y. Wang, J. Yao, Y. Wu, *Europhys. Lett.* **2014**, *106*, 60001.
- [41] A. Rehn, D. Jahn, J. C. Balzer, M. Koch, *Opt. Express* **2017**, *25*, 6712.
- [42] M.-H. Shin, W. T. Kim, S.-I. Kim, S.-H. Lee, I. C. Yu, M. Jazbinsek, W. Yoon, H. Yun, D. Kim, F. Rotermund, O.-P. Kwon, *Adv. Opt. Mater.* **2019**, *7*, 1900953.
- [43] G. A. Valdivia-Berroeta, E. W. Jackson, K. C. Kenney, A. X. Wayment, I. C. Tangen, C. B. Bahr, S. J. Smith, D. J. Michaelis, J. A. Johnson, *Adv. Funct. Mater.* **2020**, *30*, 1904786.
- [44] J. Shi, F. Liang, Y. He, X. Zhang, Z. Lin, D. Xu, Z. Hu, J. Yao, Y. Wu, *Chem. Commun.* **2019**, *55*, 7950.
- [45] S. Shang, R. Li, L. Ping, W. Luo, M. Hai, Z. Yang, D. Wang, H. Cao, W. He, *CrystEngComm* **2019**, *21*, 5626.
- [46] S.-H. Lee, M. Jazbinsek, C. P. Hauri, O.-P. Kwon, *CrystEngComm* **2016**, *18*, 7180.
- [47] E. O. Kissi, P. Bawuah, P. Silfsten, K.-E. Peiponen, *J. Infrared Milli Terahz Waves* **2015**, *36*, 278.
- [48] I. E. Gordon, L. S. Rothman, C. Hill, R. V. Kochanov, Y. Tan, P. F. Bernath, M. Birk, V. Boudon, A. Campargue, K. V. Chance, B. J. Drouin, J.-M. Flaud, R. R. Gamache, J. T. Hodges, D. Jacquemart, V. I. Perevalov, A. Perrin, K. P. Shine, M.-A. H. Smith, J. Tennyson, G. C. Toon, H. Tran, V. G. Tyuterev, A. Barbe, A. G. Császár, V. M. Devi, T. Furtenbacher, J. J. Harrison, J.-M. Hartmann, A. Jolly, et al., *J. Quant. Spectrosc. Radiat. Transfer* **2017**, *203*, 3.